

Machine-Learning-Based Monitoring of Laser Powder Bed Fusion

Bodi Yuan, Gabriel M. Guss, Aaron C. Wilson, Stefan P. Hau-Riege, Phillip J. DePond, Sara McMains, Manyalibo J. Matthews, and Brian Giera*

A two-step machine learning approach to monitoring laser powder bed fusion (LPBF) additive manufacturing is demonstrated that enables on-the-fly assessments of laser track welds. First, in situ video melt pool data acquired during LPBF is labeled according to the (1) average and (2) standard deviation of individual track width and also (3) whether or not the track is continuous, measured postbuild through an ex situ height map analysis algorithm. This procedure generates three ground truth labeled datasets for supervised machine learning. Using a portion of the labeled 10 ms video clips, a single convolutional neural network architecture is trained to generate three distinct networks. With the remaining in situ LPBF data, the trained neural networks are tested and evaluated and found to predict track width, standard deviation, and continuity without the need for ex situ measurements. This two-step approach should benefit any LPBF system – or any additive manufacturing technology – where height-map-derived properties can serve as useful labels for in situ sensor data.

1. Introduction

Laser powder bed fusion (LPBF, or equivalently selective laser melting) is an additive manufacturing technology that produces metal parts, layer by layer, by melting powdered metals and alloys with a high-power laser.^[1] Considering the beneficially large set of metallic powders available to LPBF for fabricating objects of virtually any shape, the technique is versatile and ideally suited for applications such as rapid prototyping and light-weighting.^[2] The final material properties of parts made via LPBF are extremely sensitive to the powder properties^[3] (e.g., powder shape, flow characteristics, porosity, laser absorptivity,^[4,5] etc.) and laser parameters (e.g., beam size, power, scan rate, etc.).^[6,7] As such, it is a significant challenge to identify the optimal operating parameters to rapidly and reliably produce parts with the desired properties without defects.^[8] Furthermore, many types of LPBF defects arise due to inherent

variability in the powder properties,^[9] bed thickness nonuniformity,^[10] and laser parameters and scan paths that result in improper power melting.^[11] Thus, even after optimizing LPBF operating parameters and identifying suitable processing windows,^[12] rapid build qualification, improved quality, and higher production yields require methods of monitoring the melt pool and/or powder bed in situ, i.e., during a build, that enable real-time process feedback and automated quality detection.^[13,14]

The majority of LPBF process monitoring approaches rely on noncontact sensing^[15] from optical, thermal,^[16] and/or acoustic^[17,18] sensors. These sensors provide assessments of spatial and spectral features of the melt pool,^[19,20] process plume,^[21] degree of spatter,^[22–25] overhang layers,^[26] or print bed. High-

speed image sequences of the melting process,^[27] scans of the powder bed,^[10,28] beam quality,^[29] and/or thermal monitoring^[30] are all routinely collected forms of in situ monitoring data. Making use of this data requires methods that can extract relevant diagnostic information. For instance, before initiating laser melting, automated computer vision algorithms can characterize metal powder feedstocks,^[31] and image analysis of newly spread powder can reveal nonuniformities in the powder bed thickness.^[32] Aminzadeh et al. demonstrated layer-by-layer detection of fusion defects from images using a Bayesian classifier.^[33] Real-time events such as material ejecta are detectable by applying manually set thresholds to high-speed near-infrared images of the melt pool. Also, increasing the $\mu\text{m pixel}^{-1}$ image resolution relative to the standard deviation of measured track width, σ_{measured} , may result in improved predictions of the final track width, $\delta_{\text{predicted}}$, and topography.^[34] Reducing laser power proportionally to an integrated signal from a photodiode calibrated against a camera results in smoother overhang structures.^[35] Using images of the print bed taken after laser melting, a level sets method can detect intentionally created defects,^[36] machine vision algorithms can identify pore defects,^[37] and multifractal image analysis can characterize layers with balling, cracks and pores, and no defects.^[38] Visual imaging equipment is appealing to LPBF monitoring systems because it is relatively inexpensive and provides noncontact sensing.^[13]

As with most additive manufacturing systems, analysis of LPBF sensor data currently occurs postbuild, rendering

B. Yuan, G. M. Guss, Dr. A. C. Wilson, Dr. S. P. Hau-Riege, P. J. DePond, Prof. S. McMains, Dr. M. J. Matthews, Dr. B. Giera
Center for Engineered Materials and Manufacturing
Lawrence Livermore National Laboratory
P.O. Box 808, L-229, 7000 East Ave., Livermore, CA 94551, USA
E-mail: giera1@llnl.gov

 The ORCID identification number(s) for the author(s) of this article can be found under <https://doi.org/10.1002/admt.201800136>.

DOI: 10.1002/admt.201800136

process monitoring and rectification impossible.^[39] Machine learning offers a route to convert sensor data into real-time assessments; however, this requires a wealth of *labeled* sensor data that traditionally is too time consuming and/or expensive to assemble. In this manuscript, this critical issue of generating *labeled* video data for machine learning is solved. An original multistage convolutional network is trained that processes in situ high-speed video data to predict properties of track welds measured ex situ following an LPBF print. The in situ machine learning models rely on labeled time segments of high-speed video data generated from a separate height map analysis algorithm. The height map analysis algorithm presented here processes height map data of isolated track welds and extracts ground truth labels of the average and standard deviation of the width along each track and whether or not each track is continuous. A newly developed single, general convolutional architecture is trained to predict ex situ measurements from as little as 10 video frames with a correlation coefficient of $R^2 = 0.93$ for track width, $R^2 = 0.70$ for standard deviation of track width, and prediction accuracy of 93.1% for track continuity. The algorithm successfully generalizes across multiple tracks created with several combinations of the laser power and speed. In terms of broader impact, since this approach to generate labeled training sets for in situ machine-learning-based detection algorithms does not rely on specific LPBF characteristics, it should be extensible to other additive manufacturing technologies.^[40]

2. Results and Discussion

After creating and scanning all tracks, the ex situ height map analysis algorithm is used to measure the tracks. Approximately 80% of all tracks are continuous. **Figure 1** shows measured track widths for all laser speed and power combinations studied, plotted as the average value of δ_{measured} with error bars corresponding to the standard deviation of repeat width measurements. Tracks are widest at high laser powers and slow scan speeds. The trends in **Figure 1** agree with previous findings from experiments^[44–47] and simulation^[48,49] that show that the melt pool width increases with increasing laser power-to-speed ratio, i.e., increasing volumetric energy density. Error bar values show no clear trend as a function of laser parameters throughout the dataset collected. Thus, an in situ detection technique based solely on empirical fits of these data may not reliably capture natural variances within the process.

Track measurements are used as ground truth labels for each video taken during the welding process. **Figure 2** shows the exact 10 middle center-cropped frames from the in situ videos and corresponding labels that are used to train the machine learning model for four different example laser conditions in our dataset. The bright area in the center of all video frames corresponds to incandescent light emitted from the melt pool. The video capture system alignment (**Figure 3**) ensures that the center of the melt pool appears in the same location of every frame. **Figure 2** displays video segments in order of increasing δ_{measured} and σ_{measured} , in pairs of laser powers, i.e., 147.5 W (a,b) and 342.5 W (c,d), and scan speeds, i.e., 310 (a,c) and 160 mm s⁻¹ (b,d). Melt pool size and shape

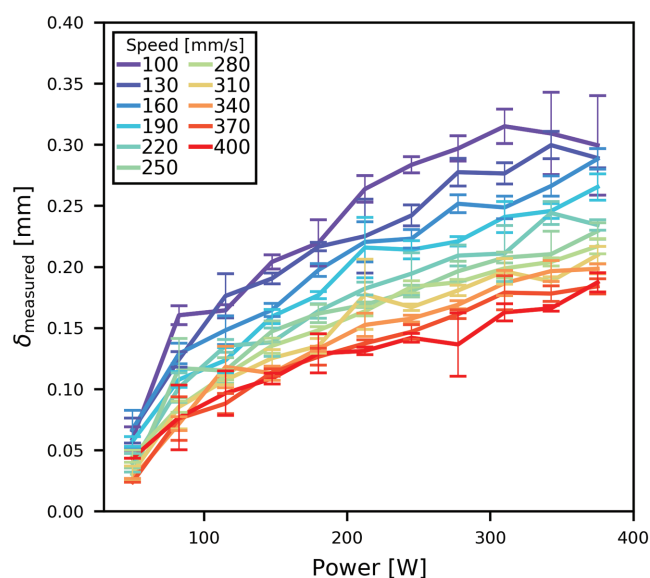


Figure 1. Measured track widths for every laser power and speed combination. The dataset exhibits an expected trend: lasers with slower speed (legend) and/or at higher power settings impart more energy into the powder bed to create wider tracks. Error bars represent the standard deviation of δ_{measured} from repeat measurements.

differences between videos at each distinct laser power setting are evident. At larger powers, the melt pool increases in size and aspect ratio, as expected. Intuitively, the relative size of the melt pool appears to correlate with larger values of δ_{measured} . Frame-by-frame variations in the quantity of bright pixels also appear to correlate with increasing σ_{measured} . For instance, there are more saturated pixels in the melt pools at high power in **Figure 2c,d** than at low power **Figure 2a,b**. The track width may also correlate with the degree of spatter, which is more pronounced for smaller δ_{measured} . It is hard to distinguish from visual inspection alone whether the melt pool is a better indicator of σ_{measured} than the spatter. In addition to these features, temporal characteristics gathered from chronological series of frames may yield accurate predictors of resulting track properties. Moreover, there may be additional salient features besides characteristics of the melt pool spatter that correlate strongly with δ_{measured} and/or σ_{measured} . It is unclear from inspection how one would identify track continuity from these video frames.

Since the relevant, visualized distinguishing features in the in situ video are not readily obvious, it is not straightforward to decipher the mapping between the video and track properties using only traditional video processing techniques. Rather than manually identifying relevant indicators within the entire in situ data set, machine learning is used to train our neural network model to learn a suitable mapping between video segments and measured average track width and standard deviation and continuity. Once trained, the CNN model generates predictions of the average track width, $\delta_{\text{predicted}}$, standard deviation, $\sigma_{\text{predicted}}$, and track continuity. The accuracy of track continuity classification is 93.1%. Regression model performance is assessed by comparing measured versus predicted values for both training and test sets in **Figure 4**. A narrow distribution of points around

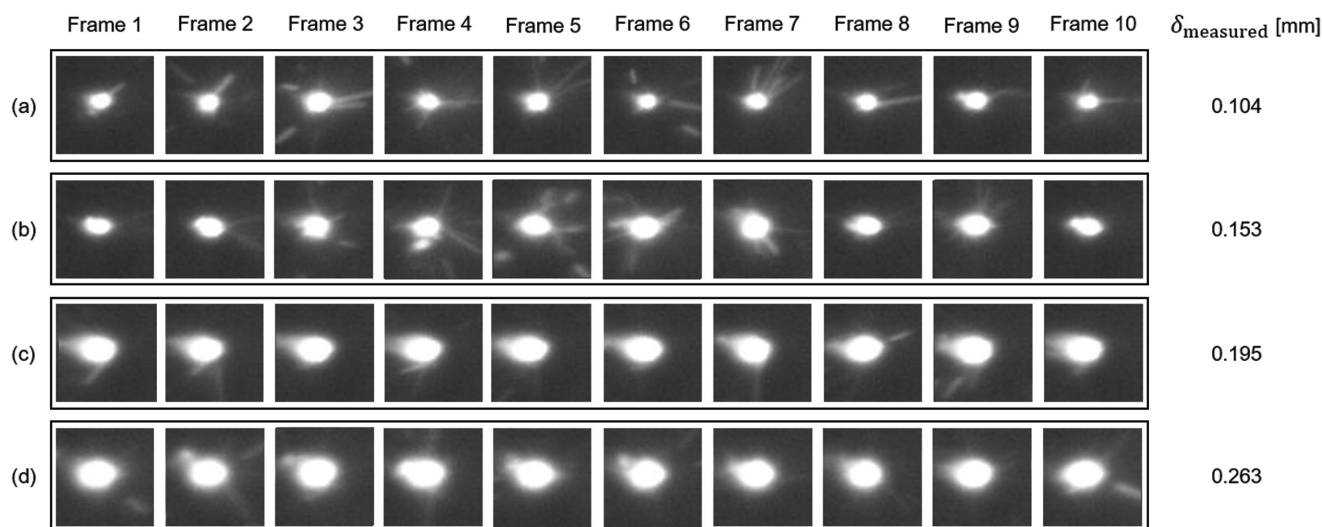


Figure 2. Machine learning training data examples: in situ LPBD video sequences with labels of measured average track width and per-pixel width standard deviation. The training process utilizes only 10 center-cropped frames from the midpoint of an LPBF video along with the measured track widths. The machine learning algorithm does not learn from the laser parameters of each video, which are 147.5 W at 310 a) and 160 b) and 342.5 W at 310 mm s⁻¹ c) and 160 mm s⁻¹ d). a) is a discontinuous track and b–d) are continuous tracks. The entire videos are provided in the Supporting Information.

the (black) line of equality indicates favorably robust model performance, while $\delta_{\text{predicted}} = \delta_{\text{measured}}$ or $\sigma_{\text{predicted}} = \sigma_{\text{measured}}$ for all predictions signifies problematic overfitting. The CNN exhibits variance, i.e., training set predictions outperform the test set, as indicated by the tighter distributions of predicted values along the equality line. Furthermore, the CNN model predictions of $\delta_{\text{predicted}}$ outperform those of $\sigma_{\text{predicted}}$ according to the respective coefficients of determination by $R_{\delta}^2 = 0.93$ and $R_{\sigma}^2 = 0.70$.

The discrepancy in model performance of predicting average track width versus standard deviation may be due only in part to the fact that the model architecture is developed using width data alone. Given the numerous available choices of model architectures and combinations of hyperparameters, different model configurations than chosen here

may result in more accurate $\sigma_{\text{predicted}}$. However, it seems likely that the standard deviation of width is inherently more difficult to predict than the width given the size and/or quality of our dataset. Outliers in Figure 4b correspond to the slowest laser scan speeds, 130 and 100 mm s⁻¹. Thus, the 10 middle frames (of the 38–50 total frames per video collected at these conditions) the model uses do not contain information of the properties along the entire length of the track. This is a consequence of the CNN architecture, which requires a fixed frame number irrespective of laser operating parameters. Recurrent neural networks that generate predictions from input videos of variable length may help to alleviate this issue. Regardless, for any machine learning model that exhibits high variance, a larger dataset ensures higher quality predictions.^[50,51] Indeed, worse results (not shown) were obtained than in Figure 4 when the model was trained on a small subset of our data. Thus, by following the experimental procedure described here, additional videos can be collected, labeled via the rapid ex situ algorithm, and used to retrain the CNN to obtain more accurate $\delta_{\text{predicted}}$, $\sigma_{\text{predicted}}$, and continuity predictions. Nevertheless, using only 10 ms videos, the CNN predicts track LPBF widths and continuity and (to a lesser degree) width standard deviation without the need for time-consuming height-map-derived ex situ measurements.

Going beyond this work, the training set can be expanded and/or the machine learning model can be modified to enable improved $\delta_{\text{predicted}}$ and $\sigma_{\text{predicted}}$ or possibly other height map derivable quality metrics, such as surface finish. In addition to detecting whether a track is defective, it is valuable to indicate where the defect occurs, which may be useful for potential rectification strategies. Moreover, it is worth pursuing whether other ex situ measurements (e.g., mechanical properties, microstructure, residual stress, part density, etc.) of LPBF printed objects are detectable from in situ data. An important requirement for in situ detection should involve

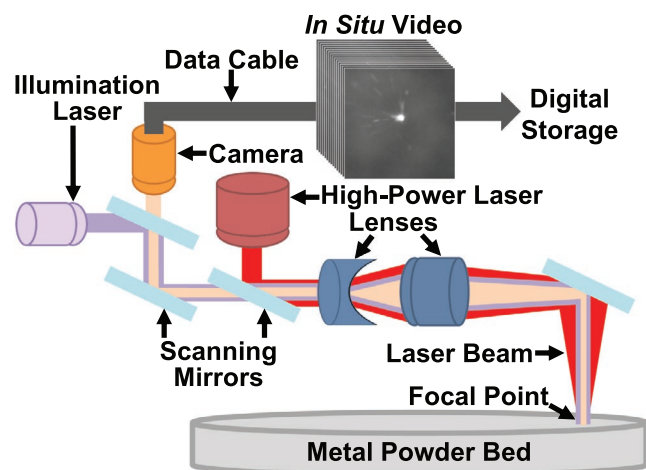


Figure 3. Schematic of video capture system. Adjustable mirrors trace the path of a focal point shared between the co-aligned high-speed camera, illumination laser, and high-power laser. The camera records in situ video taken during each welding event.

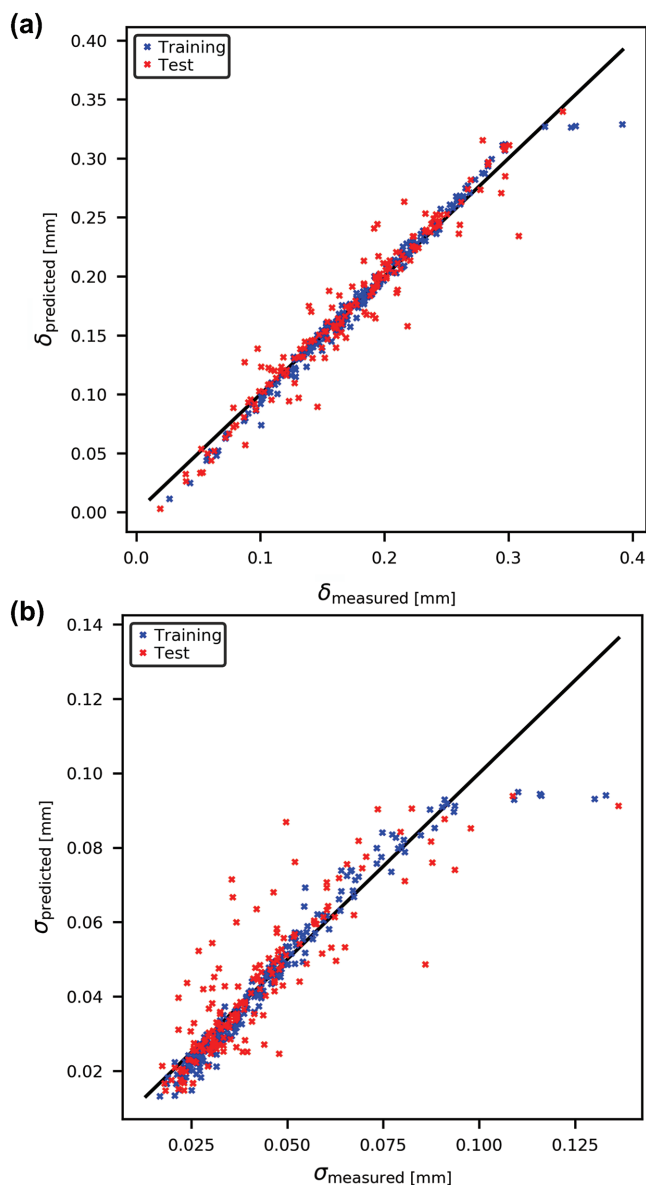


Figure 4. Predicted track widths a) and standard deviation of track width b) from 10-frame LPBF video sequences versus ex situ measured value from height maps. Predictions from the training and test sets (legend) that are close to the black line signify high accuracy. The fully-trained CNN predicts values from LPBF video with coefficients of determination $R_{\delta}^2 = 0.93$ and $R_{\sigma}^2 = 0.70$ for average track width and standard deviation of the track width, respectively.

predicting track properties in cases of multiscan prints, e.g. parallel adjacent tracks, nonparallel tracks involved in complex strategies, etc. Semisupervised or unsupervised machine learning may be necessary for cases where it is not desirable or possible to label all (or any) in situ data. Transfer learning techniques may help when ex situ measurements are difficult to obtain, e.g., X-ray computed tomography, and/or where complementary physics-based simulations are available for only a subspace of the overall operating regime. While a deeper investigation into the model may reveal something about the features it uses to make predictions, it is unlikely to uncover

important characteristics of the underlying physics of the LPBF process given the black box nature of CNNs at present. While our current model requires 10 ms video clips, faster detection rates may be possible without compromising prediction accuracy. Machine-learning-based models generated with this approach can enable in situ quality detection and real-time process monitoring essential to rapid closed-loop control.

3. Conclusions

A CNN model is developed, trained, and evaluated and shown to be capable of predicting LPBF track widths, width standard deviations, and track continuity from in situ video data alone. Here, video of LPBF tracks is collected using a variety of laser power and scan speed settings; however, it is straightforward to incorporate additional forms of in situ data, e.g., pyrometer readings, acoustic sensing, etc., that may boost prediction quality. Irrespective of the exact LPBF system configuration and/or chosen operating parameters, in situ data can be labeled using our ex situ height map analysis algorithm. After labeling in situ datasets with ex situ measurements, the model is then trained via supervised machine learning that can predict the final properties of LPBF track welds on-the-fly. With this approach, it should be possible to label in situ data via ex situ measurements for additive manufacturing technologies, e.g., extrusion-based and stereolithographic approaches, other than LPBF.

4. Experimental Section

Bead-on-plate LPBF experiments were performed wherein 870 isolated 5 mm track welds were created under a variety of randomly chosen laser speed and power settings while simultaneously recording video. After unwelded powder was removed, height maps of bare laser tracks were generated and analyzed with a novel height map analysis algorithm to determine the per-pixel average track width, δ_{measured} , standard deviation of the track width, σ_{measured} , and give each track a Boolean “continuity label” that identified whether or not a track was continuous. Each video was assigned three labels and assembled into training sets for our machine learning algorithm. A single supervised machine learning architecture was used to predict these three ex situ measurements from in situ video data, as described below.

An Aconity LAB system from Aconity3D was used for welding single tracks of 316L stainless steel. The system used a carbon fiber brush to spread metal powder evenly into a $\approx 50 \mu\text{m}$ layer atop a 180 mm 316L stainless steel plate in an argon-purged environment. Galvanometer mirrors scanned the high-power laser across evenly spaced track sites on the powder bed at 11 possible scan speeds and 11 possible laser powers in evenly spaced increments between $100\text{--}400 \text{ mm s}^{-1}$ and $50\text{--}375 \text{ W}$, respectively, with each set of laser conditions repeated up to seven times. In situ video data were recorded at frame rate of 1 kHz and frame size of 256×256 pixels using a 10 bit Mikrotrotron EOSens MC1362 incorporated into the optical system diagrammed in Figure 3. The illumination laser and Mikrotrotron video camera were co-aligned with the high-power laser. These components shared a common moving focal point, fixed at the melt pool while the laser scans each track site. In each video, the melt pool and spatter were visible for each frame. The total frames per video ranged from 12 to 50 frames, depending on the laser scan speed. The camera pixel size was $14 \mu\text{m pixel}^{-1}$.

Upon completing the bead-on-plate experiment, unwelded powder was removed from the plate and a Keyence VR3000 3D macroscope was used to generate a height map of all laser tracks. Figure 5a shows

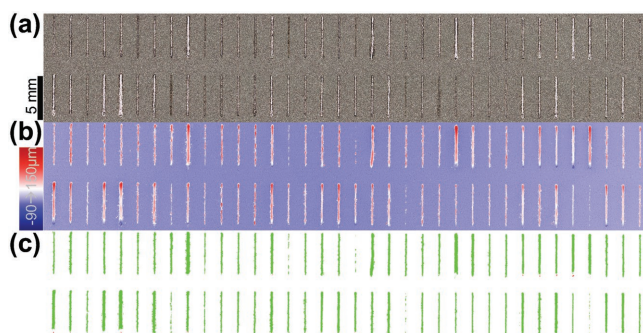


Figure 5. Ex situ analysis of laser track height maps. a) Electro-optical image of tracks weld on bare plate and corresponding height map b). c) results from applying the ex situ height map analysis algorithm that classifies each pixel as track, etch, or background, colored green, red, and white, respectively. From c), per-pixel track width average, δ_{measured} , and standard deviation, σ_{measured} , and continuity are determined.

the grayscale electro-optical image of an array of isolated track welds. Structured light scans from the Keyence VR3000 instrument measured the height at each pixel in order to produce a surface map as shown in Figure 5b. Our pixel-level classification algorithm distinguished track from background as shown in Figure 5c. After applying our classification algorithm, any number of quality metrics could be calculated from a surface map, e.g., δ_{measured} , σ_{measured} , whether or not the track was continuous, surface roughness, etc., by de-noising the height data, distinguishing track from background, and analyzing the height values corresponding to the track. This paper focused solely on the prediction of the mean and standard deviation of track widths and classification of track continuity with our proposed algorithm.

From the height maps, pixels were classified as one of three types: track weld, background, or etch (in which the height map gives values below the background). Since track locations were specified with preset spacing in both the horizontal and vertical directions, it was straightforward to analyze individual tracks in rectangular patches that encompassed the track and surrounding background. In each patch, background pixels were removed so that only weld and etch pixels remained via the following protocol:

1. Calculated the mean pixel height in each patch, h_1 .
2. Identified pixels whose heights were within $h_1 \pm \iota$, where ι is a small constant with default value 0.01 mm. Pixels within this range were likely to belong to the track weld.
3. Calculated the mean height for pixels outside of this range, h_2 . Pixels whose heights were within $h_2 \pm \iota$ belonged to the background. The remaining pixels were given a preliminary classification of nonbackground.

After executing the steps above, a binary {background, nonbackground} map was obtained that might contain mistakenly classified pixels due to the specified value of ι and inherent noise. Such “noise” pixels appeared as small isolated regions on the height map that did not manifest in the electro-optical images. To filter these noise pixels, suspected noise pixels per column of pixels were counted in a given patch and reclassified as background if that count, n , was below some threshold. Here $n = 10$, which was $\approx 6\%$ of the overall track length. Etch pixels corresponded to negative height values that resulted from the laser etching into the plate. After de-noising, a postprocessed height map identified track, etch, and background, as shown in Figure 5c. From the postprocessed height map, δ_{measured} and σ_{measured} were computed for every track and these were used to assign ground truth labels for the corresponding in situ videos, thereby assembling a training set for two regression models. Each track was also assessed for continuity, i.e., a track was discontinuous if at least one gap of nontrack pixels existed along its length, otherwise a track was continuous. The continuity labels served as a training set for a binary classification model. The entire plate

was scanned in less than 4 h and the ex situ height map analysis ran in <10 s. Since a large training set of in situ LPBF data was amassed quickly, it was feasible to develop machine learning algorithms capable of assessing the in situ data.

The LPBF video dataset contained 870 individual videos, labeled according the ex situ height map analysis algorithm that provided each video a label of δ_{measured} and σ_{measured} for regression, and tracked continuity for classification. To do this, 700 randomly selected videos were used to train candidate machine learning models and the remaining videos were used to test the fully trained models. The standard mean squared error loss function was used for the regression predictions, while cross entropy loss was used for classification. The model architecture was developed using only the δ_{measured} labels, but was trained separately on all three labels, and the learning rate hyperparameter retuned. Our CNN architecture required videos to be a fixed frame length and resolution. For the fastest scan speed, there were only 12 frames of video and the first and last frames were omitted to ensure end-of-track artifacts did not affect the results. Thus, only the 10 middle frames were chosen from each video, i.e., middle 10 ms of video. Furthermore, the frames for each track were center-cropped into 64×64 pixel size images, eliminating a portion of the background from the videos so that the neural network trained on the most relevant region of the video that encompassed the laser spot. A CNN^[41,42] was used to address this regression or classification problem. The CNN model was configured and trained with the TensorFlow^[43] library on an NVIDIA TITAN X GPU. A full description of the CNN model architecture and training hyperparameters is given in the Supporting Information; below, the most important features of our model are discussed.

To set the number of layers (the depth of the model), an initial architecture was configured with six convolutional layers, which contained sufficient capacity to learn δ_{measured} from the video data. Then the number of layers was reduced sequentially until the model did not exhibit overfitting. (Overfitted models provided excellent predictions for a training set, but did not generalize well to new datasets.) Based on several candidate model training sessions, three convolutional layers could generalize sufficiently to the test data. Although it was more common to use max-pooling to reduce dimensionality between convolutional layers, mean-pooling was found to outperform max-pooling for learning to predict the track width. For this application, mean-pooling might help the CNN learn about the differences in melt pool size to generate predictions for the track width average, $\delta_{\text{predicted}}$. If this was the case, the overall summation of the video pixel values would seem to be more relevant than the summation of max pixel values. Though the model architecture was not optimized based on track continuity or standard deviation of width measurements, reasonable results were obtained when retraining the same CNN model (developed with δ_{measured}) using σ_{measured} and continuity labels.

Supporting Information

Supporting Information is available from the Wiley Online Library or from the author.

Acknowledgements

This work was performed under the auspices of the U.S. Department of Energy by Lawrence Livermore National Laboratory under Contract DE-AC52-07NA27344, LLNL-JRNL-748383. This work was also supported by a Berkeley Graduate Fellowship. This article is part of the special series on *Advanced Intelligent Systems* that showcases the outstanding achievements of leading international researchers on intelligent systems.

Conflict of Interest

The authors declare no conflict of interest.

Keywords

additive manufacturing, laser powder bed fusion, machine learning, selective laser melting

Received: April 26, 2018

Revised: July 19, 2018

Published online:

- [1] C. Y. Yap, C. K. Chua, Z. L. Dong, Z. H. Liu, D. Q. Zhang, L. E. Loh, S. L. Sing, *Appl. Phys. Rev.* **2015**, 2, 041101.
- [2] W. E. Frazier, *J. Mater. Eng. Perform.* **2014**, 23, 1917.
- [3] J. A. Slotwinski, E. J. Garboczi, P. E. Stutzman, C. F. Ferraris, S. S. Watson, M. A. Peltz, *J. Res. Natl. Inst. Stand. Technol.* **2014**, 119, 460.
- [4] C. D. Boley, S. C. Mitchell, A. M. Rubenchik, S. S. Q. Wu, *Appl. Opt.* **2016**, 55, 6496.
- [5] A. Rubenchik, S. Wu, S. Mitchell, I. Golosker, M. LeBlanc, N. Peterson, *Appl. Opt.* **2015**, 54, 7230.
- [6] C. Kamath, *Int. J. Adv. Manuf. Tech.* **2016**, 86, 1659.
- [7] C. Kamath, B. El-dasher, G. F. Gallegos, W. E. King, A. Sisto, *Int. J. Adv. Manuf. Tech.* **2014**, 74, 65.
- [8] A. Bauereiß, T. Scharowsky, C. Körner, *J. Mater. Process. Technol.* **2014**, 214, 2522.
- [9] J.-P. Choi, G.-H. Shin, H.-S. Lee, D.-Y. Yang, S. Yang, C.-W. Lee, M. Brochu, J.-H. Yu, *Mater. Trans.* **2017**, 58, 294.
- [10] L. Scime, J. Beuth, *Addit. Manuf.* **2018**, 19, 114.
- [11] T. DebRoy, H. L. Wei, J. S. Zuback, T. Mukherjee, J. W. Elmer, J. O. Milewski, A. M. Beese, A. Wilson-Heid, A. De, W. Zhang, *Prog. Mater. Sci.* **2018**, 92, 112.
- [12] G. Tapia, S. Khairallah, M. Matthews, W. E. King, A. Elwany, *Int. J. Adv. Manuf. Technol.* **2018**, 94, 3591.
- [13] T. G. Spears, S. A. Gold, *IMMI* **2016**, 1.
- [14] S. K. Everton, M. Hirsch, P. Stravroulakis, R. K. Leach, A. T. Clare, *Mater. Des.* **2016**, 95, 431.
- [15] H. Kim, Y. Lin, T.-L. B. Tseng, *Rapid Prototyping J.* **2018**, 24, 00.
- [16] T. Purtonen, A. Kalliosaari, A. Salminen, *Phys. Procedia* **2014**, 56, 1218.
- [17] K. Wasmer, C. Kenel, C. Leinenbach, S. A. Shevchik, in *Ind. Addit. Manuf. – Proc. Addit. Manuf. Prod. Appl. – AMPA2017* (Eds.: M. Meboldt, C. Klahn), Springer International Publishing, Cham, **2018**, pp. 200–209.
- [18] S. A. Shevchik, C. Kenel, C. Leinenbach, K. Wasmer, *Addit. Manuf.* **2017**, 21, <https://doi.org/10.1016/j.addma.2017.11.012>.
- [19] S. Berumen, F. Bechmann, S. Lindner, J.-P. Kruth, T. Craeghs, *Phys. Procedia* **2010**, 5, 617.
- [20] M. A. Doubenskaia, I. V. Zhirnov, V. I. Teleshevskiy, P. Bertrand, I. Y. Smurov, *Mater. Sci. Forum* **2015**, 834, 93.
- [21] M. Grasso, A. G. Demir, B. Previtali, B. M. Colosimo, *Robot. Comput.-Integr. Manuf.* **2018**, 49, 229.
- [22] S. Ly, A. M. Rubenchik, S. A. Khairallah, G. Guss, M. J. Matthews, *Sci. Rep.* **2017**, 7, 4085.
- [23] H. Nakamura, Y. Kawahito, K. Nishimoto, S. Katayama, *J. Laser Appl.* **2015**, 27, 032012.
- [24] H. Park, S. Rhee, D. Kim, *Meas. Sci. Technol.* **2001**, 12, 1318.
- [25] V. Gunenthiram, P. Peyre, M. Schneider, M. Dal, F. Coste, I. Koutiri, R. Fabbro, *J. Mater. Process. Technol.* **2018**, 251, 376.
- [26] Y. Chivel, *Phys. Procedia* **2013**, 41, 904.
- [27] A. Gusarov, D. Kotoban, I. Zhirnov, *MATEC Web Conf.* **2017**, 129, 01037.
- [28] V. Forbes, J. A. Alvarez, R. M. Califa, S. J. Ezersky, G. A. L. Quiroz, K. L. Zeng, G. C. Lewin, *IEEE Systems and Information Engineering Design Symposium (SIEDS)* **2017**, pp. 225–230.
- [29] C. Dini, *Laser Tech. J.* **2018**, 15, 35.
- [30] J. Li, R. Jin, H. Z. Yu, *Mater. Des.* **2018**, 139, 473.
- [31] B. L. DeCost, H. Jain, A. D. Rollett, E. A. Holm, *JOM* **2017**, 69, 456.
- [32] T. Craeghs, S. Clijsters, E. Yasa, J.-P. Kruth, in *Proceedings of the Solid Freeform Fabrication Symposium*, Austin, TX **2011**, pp. 212–226.
- [33] M. Aminzadeh, T. R. Kurfess, *J. Intell. Manuf.* **2018**, <https://doi.org/10.1007/s10845-018-1412-0>.
- [34] J. C. Fox, B. M. Lane, H. Yeung, in *SPIE Commer. Sci. Sens. Imaging* (Eds.: P. Bison, D. Burleigh), International Society For Optics And Photonics, Anaheim, California, USA **2017**, pp. 1021407–1021407.
- [35] J.-P. Kruth, J. Duflou, P. Mercelis, J. Van Vaerenbergh, T. Craeghs, J. De Keuster, in *Proc. 5th Lane Conf. Laser Assist. Net Shape Eng.* (Eds.: M. Geiger, A. Otto), Bamberg, Germany **2007**, pp. 23–37.
- [36] M. Abdelrahman, E. W. Reutzel, A. R. Nassar, T. L. Starr, *Addit. Manuf.* **2017**, 15, 1.
- [37] M. Aminzadeh, *A Machine Vision System for In-Situ Quality Inspection in Metal Powder-Bed Additive Manufacturing*, Georgia Institute of Technology, Atlanta, Georgia, USA **2016**.
- [38] B. Yao, F. Imani, A. S. Sakpal, E. W. Reutzel, H. Yang, *J. Manuf. Sci. Eng.* **2018**, 140, 031014.
- [39] J. Stavridis, A. Papacharalampopoulos, P. Stavropoulos, *Int. J. Adv. Manuf. Technol.* **2018**, 94, 1825.
- [40] B. Giera, *Rapid Closed-Loop Control Based on Machine Learning*, US20170144378A1, **2015**.
- [41] Y. LeCun, Y. Bengio, G. Hinton, *Nature* **2015**, 521, 436.
- [42] A. Krizhevsky, I. Sutskever, G. E. Hinton, *Commun. ACM* **2017**, 60, 84.
- [43] M. Abadi, P. Barham, J. Chen, Z. Chen, A. Davis, J. Dean, M. Devin, S. Ghemawat, G. Irving, M. Isard, M. Kudlur, J. Levenberg, R. Monga, S. Moore, D. G. Murray, B. Steiner, P. Tucker, V. Vasudevan, P. Warden, M. Wicke, Y. Yu, X. Zheng, *Proceedings of the 12th USENIX Symposium on OSDI* **2016**, 16, pp. 265–283.
- [44] C. Kusuma, S. H. Ahmed, A. Mian, R. Srinivasan, *J. Mater. Eng. Perform.* **2017**, 26, 3560.
- [45] C. Kusuma, *The Effect of Laser Power and Scan Speed on Melt Pool Characteristics of Pure Titanium and Ti-6Al-4 V Alloy for Selective Laser Melting*, *Browse All Theses and Dissertations*, Wright State University, **2016**.
- [46] I. Yadroitsev, A. Gusarov, I. Yadroitsava, I. Smurov, *J. Mater. Process. Technol.* **2010**, 210, 1624.
- [47] I. Yadroitsev, P. Bertrand, I. Smurov, *Appl. Surf. Sci.* **2007**, 253, 8064.
- [48] S. A. Khairallah, A. Anderson, *J. Mater. Process. Technol.* **2014**, 214, 2627.
- [49] S. A. Khairallah, A. T. Anderson, A. Rubenchik, W. E. King, *Acta Mater.* **2016**, 108, 36.
- [50] A. Halevy, P. Norvig, F. Pereira, *IEEE Intell. Syst.* **2009**, 24, 8.
- [51] M. Banko, E. Brill, *Proceedings of the 39th annual meeting on association for computational linguistics*, Association For Computational Linguistics, Stroudsburg, PA, USA **2001**, pp. 26–33.